Accepted Article

Title: Design of Ultra-Narrow Bandgap Polymer Acceptors for High-Sensitivity Flexible All-Polymer Short-Wavelength Infrared Photodetectors

Authors: Xiaofeng Chen, Yu Zhu, Yan Xu, Mei Rao, Pengfei Pang, Bo Zhang, Chenhui Xu, Wang Ni, Guanghui Li, Jishan Wu, Miaomiao Li, Yongsheng Chen, and Yanhou Geng

WILEY VCH

RESEARCH ARTICLE

Design of Ultra-Narrow Bandgap Polymer Acceptors for High-Sensitivity Flexible All-Polymer Short-Wavelength Infrared Photodetectors

Xiaofeng Chen, [a][b][c] Yu Zhu,[d] Yan Xu,[a] Mei Rao,[a] Pengfei Pang,[a][b][c] Bo Zhang,[a] Chenhui Xu,[a] Wang Ni,[e] Guanghui Li*[d], Jishan Wu*[b][c], Miaomiao Li*[d], Yongsheng Chen,[d] and Yanhou Geng[a][b]

[a]   X. Chen, Y. Xu, M. Rao, P. Pang, B. Zhang, C. Xu, Dr. M. Li, Prof. Y. Geng
        School of Materials Science and Engineering, Tianjin Key Laboratory of Molecular Optoelectronic Science and Key Laboratory of Organic Integrated
        Circuits, Ministry of Education, Tianjin University, Collaborative Innovation Center of Chemical Science and Engineering (Tianjin), Tianjin, 300072, China
        E-mail: miaomiao.li@tju.edu.cn
[b]   X. Chen, P. Pang, Prof. J. Wu, Prof. Y. Geng
        Joint School of National University of Singapore and Tianjin University, International Campus of Tianjin University, Binhai New City, Fuzhou, 350507, China
[c]   X. Chen, P. Pang, Prof. J. Wu
        Department of Chemistry, National University of Singapore, 3 Science Drive 3, 117543 Singapore, Singapore
        E-mail: chmwuj@nus.edu.sg
[d]   Y. Zhu, Dr. G. Li, Prof. Y. Chen
        The Centre of Nanoscale Science and Technology and Key Laboratory of Functional Polymer Materials, Institute of Polymer Chemistry, Tianjin Key
        Laboratory of Functional Polymer Materials, College of Chemistry, and Renewable Energy Conversion and Storage Center, Nankai University, Tianjin
        300071, China.
        E-mail: ghli1127@nankai.edu.cn
[e]   Dr. W. Ni
        Science and Technology on Power Sources Laboratory, Tianjin Institute of Power Sources, Tianjin, 300384, China.

Abstract: All-polymer photodetectors possess unique mechanical flexibility and are ideally suitable for the application in next-generation flexible, wearable short-wavelength infrared (SWIR, 1000–2700 nm) photodetectors. However, all-polymer photodetectors commonly suffer from low sensitivity, high noise, and low photoresponse speed in the SWIR region, which significantly diminish their application potential in wearable electronics. Herein, two polymer acceptors with absorption beyond 1000 nm, namely P4TOC-DCBT and P4TOC-DCBSe, were designed and synthesized. The two polymers possess rigid structure and good conformational stability, which is beneficial for reducing energetic disorder and suppressing dark current. Owing to the efficient charge generation and ultralow noise current, the P4TOC-DCBT-based all-polymer photodetector achieved a specific detectivity (D^*) of over 10^{12} Jones from 650 (visible) to 1070 nm (SWIR) under zero bias, with a response time of 1.36 µs. These are the best results for reported all-polymer SWIR photodetectors in photovoltaic mode. More significantly, the all-polymer blend films exhibit good mechanical durability, and hence the P4TOC-DCBT-based flexible all-polymer photodetectors show a small performance attenuation (<4%) after 2000 cycles of bending to a 3 mm radius. The all-polymer flexible SWIR organic photodetectors are successfully applied in pulse signal detection, optical communication and image capture.

Introduction

Owing to the high transmittance of body tissues and atmosphere to short-wavelength infrared (SWIR) light (1000–2700 nm), SWIR photodetectors have attracted widespread attention in remote sensing, three-dimensional vision, optical communication, health monitoring, etc.[1-3] Currently, commercially available SWIR photodetectors mainly rely on crystalline inorganic semiconductors, such as germanium (Ge) and group III–V compounds. These inorganic SWIR photodetectors suffer from mechanical rigidity, complicated fabrication processes,[4] fixed bandgap and high cost, which restrict their applications in typical burgeoning fields like wearable electronics, soft robotics, prosthetics, and implanted electronics. In contrast, organic photodetectors (OPDs) with a bulk-heterojunction active layer composed of donor and acceptor materials exhibit solution processability, intrinsic flexibility, tailorable bandgap and non-toxicity. Over the past few years, OPDs based on a polymer donor with a fullerene or small molecule acceptor (SMA) have significantly advanced and currently exhibit high-sensitivity photodetection beyond 1000 nm.[5-14] All-polymer SWIR OPDs, comprising polymer donors and acceptors, offer additional merits such as remarkable mechanical stretchability, excellent morphological stability and suitability for industrial manufacturing.[15-18] These characteristics make them ideal candidates for constructing next-generation lightweight and wearable SWIR photodetectors that can be adhered to human skin for physiological monitoring or to curved surfaces for optical communication, image sensing, etc. Unfortunately, state-of-the-art all-polymer OPDs commonly exhibit low sensitivity in the SWIR region, high noise and low photoresponse speed. The major bottleneck lies in the lack of all-polymer semiconductor systems with efficient SWIR light absorption and charge generation. Moreover, it is essential although challenging to attain low energy disorders and trap states in all-polymer blends via molecular and device engineering, which can significantly improve the sensitivity and photoresponse speed of SWIR OPDs.

In theory, ultra-narrow-bandgap (ultra-NBG) polymers can act as either a donor or acceptor in OPDs, depending on their frontier

RESEARCH ARTICLE

molecular orbital (FMO) levels and carrier transport characteristics. Ultra-NBG polymers can be obtained by significantly upshifting the highest occupied molecular orbital (HOMO) or downshifting the lowest unoccupied molecular orbital (LUMO) levels. Nevertheless, donor polymers with high HOMO levels are prone to oxidation in air, whereas greatly downshifting the LUMO level of the donor may impede hole transport. In contrast, narrowing the bandgap of acceptor polymers by greatly downshifting the LUMO level has no negative impact on chemical

stability and electron transport. The success of non-fullerene organic solar cells (OSCs)[19-21] and SWIR OPDs based on ultra-NBG SMAs[7-11] also proves the key role of NBG acceptor molecules in attaining high photocurrent. However, few studies on designing and synthesizing high-performance ultra-NBG polymer acceptors for all-polymer OPDs have been reported. Thus, ultra-NBG polymer acceptors that cooperate well with existing polymer donors must be urgently developed for the realization of high-performance SWIR OPDs.
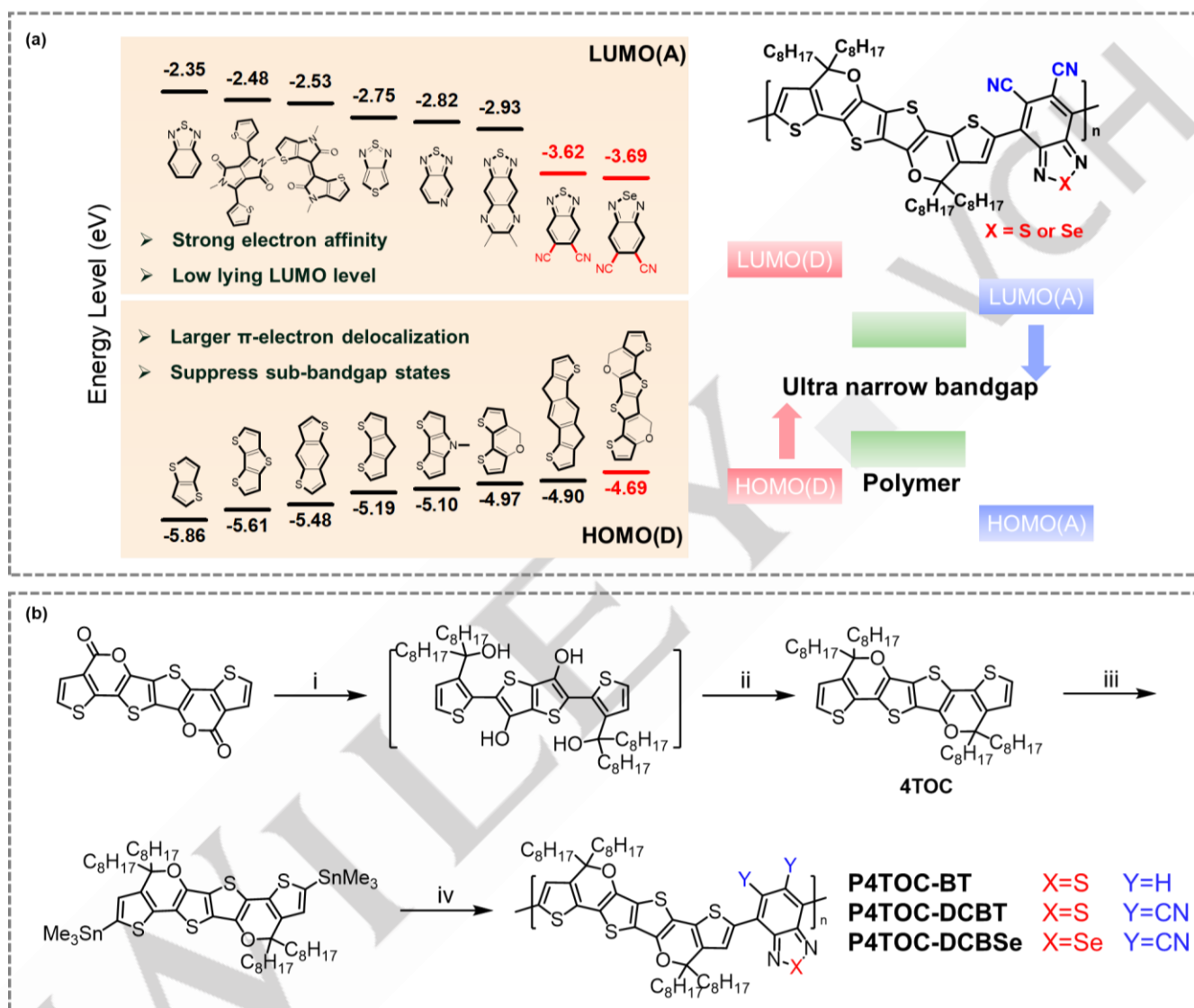
Scheme 1. (a) Calculated LUMO levels of the commonly used acceptor units and HOMO levels of electron-rich fused rings. The HOMO and LUMO levels were calculated using DFT at the B3LYP/6-31-G (d) level. (b) Synthetic route for the preparation of P4TOC-BT, P4TOC-DCBT and P4TOC-DCBSe. (i) $C_8H_{17}MgBr$, Et_2O, -78 °C to 25 °C; (ii) PTSA, toluene, 110 °C; (iii) n-BuLi, $SnMe_3Cl$, THF, -78 °C; (iv) P(t-Bu)$_3$ Pd G3, K_3PO_4, THF, 35 °C.

Typical electron-deficient units such as benzothiadiazole (BT) and its derivatives are widely used for constructing polymer acceptors for OSCs.[22-28] Comprehensive works reveal that the introduction of cyano (CN) groups into BT in the polymer repeating units can substantially downshift the LUMO level but only slightly reduce the HOMO level, thereby causing the red-shifting of the absorption band by ~200 nm.[29-33] According to density functional theory (DFT) calculations (Scheme 1a), the

LUMO level of dicyano-substituted benzothiadiazole (DCBT) is lower than those of the commonly used electron-deficient units, suggesting that DCBT is a promising acceptor unit for the construction of polymer acceptors with ultra-NBG and deep FMOs. Based on the molecular design of high-efficiency non-fullerene acceptors in OSCs, electron-rich conjugated fused rings should be appropriate donor moieties. Their rigid and planar molecular structures and large π-electron delocalization have been proven

RESEARCH ARTICLE

to play a crucial role in yielding appropriate morphology for suppressing energy disorder and sub-bandgap states,[34-38] which is beneficial for reducing dark current. Among the fused ring units, the carbon-oxygen-bridged fused ring, 1,1'-[2,5-dithiophen-2-ylfuran-3,4-diyl]bis[heptadecane] (4TOC) shows very strong electron-donating ability (Scheme 1a), which contributes to the enhancement of intramolecular charge transfer and broadening of light absorption. Consequently, the copolymerization of 4TOC with DCBT or its derivatives should be a feasible strategy to obtain ultra-NBG acceptor polymers.

Herein, we designed and synthesized two polymers, i.e. P4TOC-DCBT and P4TOC-DCBSe (Scheme 1), using DCBT and dicyano-substituted benzoselenidazole (DCBSe) as acceptor moieties and alkyl-substituted 4TOC as a donor moiety. For comparison, a polymer based on 4TOC and BT units, named P4TOC-BT, was also synthesized and characterized. P4TOC-DCBT and P4TOC-DCBSe exhibit downshifted FMOs and decreased optical bandgaps of 1.13 and 0.99 eV, respectively, compared to P4TOC-BT. Moreover, the incorporation of CN switches the dominant transport characteristic of the polymers from p-type to n-type (or bipolar characteristics), and stabilize the conformation of the polymer backbone, which is beneficial for reducing energetic disorder and trap density. Using ultra-NBG polymers (P4TOC-DCBT and P4TOC-DCBSe) as acceptors, we fabricated high-speed self-powered all-polymer OPDs capable of sensitive photodetection ranging from visible light to the SWIR region. The dark current of P4TOC-DCBT based all-polymer OPDs was effectively suppressed to an ultralow level of 1.7×10^{-11} A/cm². As a result, P4TOC-DCBT based device exhibited a high shot-noise limited specific detectivity (D_{sh}^*) surpassing 10^{13} Jones from 610 (visible) to 1080 nm (WSIR), and a remarkable specific detectivity (D^*) over 10^{12} Jones from 650 (visible) to 1070 nm (SWIR) under zero bias, marking a significant milestone for all-polymer SWIR OPDs. In addition, P4TOC-DCBT based photodetector presented a long-term thermal and air stabilities, and fast response speed with a response time of 1.36 μs, which is the best performance among the all-polymer OPDs reported so far. Owing to the exceptional stretchability of the all-polymer blend films, the P4TOC-DCBT-based flexible OPDs exhibited negligible decline in detectivity after 2000 cycles of repeated bending to a radius of 3 mm. Furthermore, the all-polymer flexible OPDs were successfully applied in heart rate monitoring, optical communication and SWIR imaging. This study opens a promising avenue to develop flexible and wearable SWIR photodetectors based on all-polymer semiconductors.

Results and Discussion

Synthesis, DFT Calculations and Material Properties.

The synthetic route to the monomer and polymers is shown in Scheme 1b. Detailed information regarding the synthesis of the monomer and polymers is provided in the Supporting Information. Thieno[2,3-d]thieno[3,2-b]pyrano[2',3':5,6]pyrano[4,3-b]thieno[3,2-d]pyran-4,10-dione (fused-ring lactone) was synthesized according to the literature.[39-41] 4TOC was obtained by adding six equivalents of *n*-octylmagnesium bromide to the fused-ring

lactone followed by an intramolecular dehydration cyclization, with a two-step yield of 60%. Subsequently, 4TOC reacted with trimethyltin to afford distannylated 4TOC, with a yield of 81%. The structures of intermediates and monomers were characterized by NMR spectroscopy and matrix-assisted laser desorption/ionization time-of-flight (MALDI-TOF) mass spectrometry (Figure S1-S6). Given that distannylated 4TOC is sensitive to high temperature and oxygen, the polymers were obtained by copolymerizing distannylated 4TOC with dibrominated BT, DCBT and DCBSe monomers, respectively, via Stille coupling at room temperature to reduce by-products and defects. The structures of the polymers were confirmed by high-temperature NMR (Figures S7-S9). All polymers exhibit good solubility in most common organic solvents like chloroform and chlorobenzene. The number average molecular weight (M_n) and polydispersity index (PDI) are 17.5 kDa and 1.43 for P4TOC-BT, 14.5 kDa and 1.78 for P4TOC-DCBT, and 16.2 kDa and 1.47 for P4TOC-DCBSe, respectively, as measured by gel permeation chromatography (GPC) with polystyrene as the standard and THF as the eluent at 40 ℃ (Figure S10). Thermogravimetric analyses indicate the excellent thermal stability of the three polymers, with decomposition temperatures (T_d, with 5% weight loss) above 320 ℃ (Figure S11).

The wavefunction distribution of FMOs and molecular geometry of the polymers were investigated through DFT calculations. As shown in Figure S12, the HOMOs of the three polymers are distributed along the entire conjugated backbones, whereas the LUMOs are mainly localized at the acceptor units. The calculated HOMO/LUMO energy levels of the trimers are −4.45/−2.83, −4.84/−3.54 and −4.83/−3.53 eV for P4TOC-BT, P4TOC-DCBT and P4TOC-DCBSe, respectively. Thus, the introduction of CN groups into the BT unit causes a greater downshift in the LUMO level than in the HOMO level, significantly reducing in the calculated bandgaps. To elucidate the narrowing of bandgaps, the D-A effect and the quinoidal resonance effect were assessed using frontier orbital charge density difference[42-45] and bond length alternation (BLA)[46-49]. As shown in Figure 1a, a peak-valley-peak characteristic pattern observed along the longest direction of molecular backbones is more pronounced in P4TOC-DCBT and P4TOC-DCBSe than in P4TOC-BT, indicating a greater D–A effect in the former two compounds. BLA values, as a gauge of the quinoidal resonance effect, are 0.028 and 0.032 Å for P4TOC-DCBT and P4TOC-DCBSe, respectively (Figure S13), similar to that of P4TOC-BT (0.033 Å). These results imply the significantly decreased bandgaps for P4TOC-DCBT and P4TOC-DCBSe mainly originated from the enhanced D-A effect. The DFT optimized molecular geometries of the polymers are shown in Figure 1b. Compared to P4TOC-BT, P4TOC-DCBT and P4TOC-DCBSe show larger torsion angles of 22° and 20° between the acceptor moiety and adjacent 4TOC unit, due to the steric hindrance of the CN group. The relaxed potential surface energy scans were performed to evaluate the conformational stabilities of the rotatable C–C bonds between 4TOC and BT derivatives (Figure 1c). The energy difference between the stable and meta-stable states (ΔE_{s-ms}) for P4TOC-DCBT and P4TOC-DCBSe is about twice as high as that for P4TOC-BT, derived from

3

RESEARCH ARTICLE

the steric hindrance of the CN group. The torsional energy barrier from stable state to meta-stable state ($E_{s\text{-}ms}$) for P4TOC-BT is the highest among the three polymers. The high $E_{s\text{-}ms}$ and the low $\Delta E_{s\text{-}ms}$ for P4TOC-BT should be related to the conformational locks involving [N···H], [S···H] and [N···S] non-covalent interactions (as shown in Figure S12b) in both stable and metastable molecular conformations. These results indicate that P4TOC-DCBT and

P4TOC-DCBSe have better conformational stability, which are beneficial for enhancing intermolecular interactions and reducing energetic disorder. The stronger intermolecular interactions of P4TOC-DCBT and P4TOC-DCBSe were evidenced by the higher disaggregation temperatures of P4TOC-DCBT and P4TOC-DCBSe in solution, which will be discussed below.
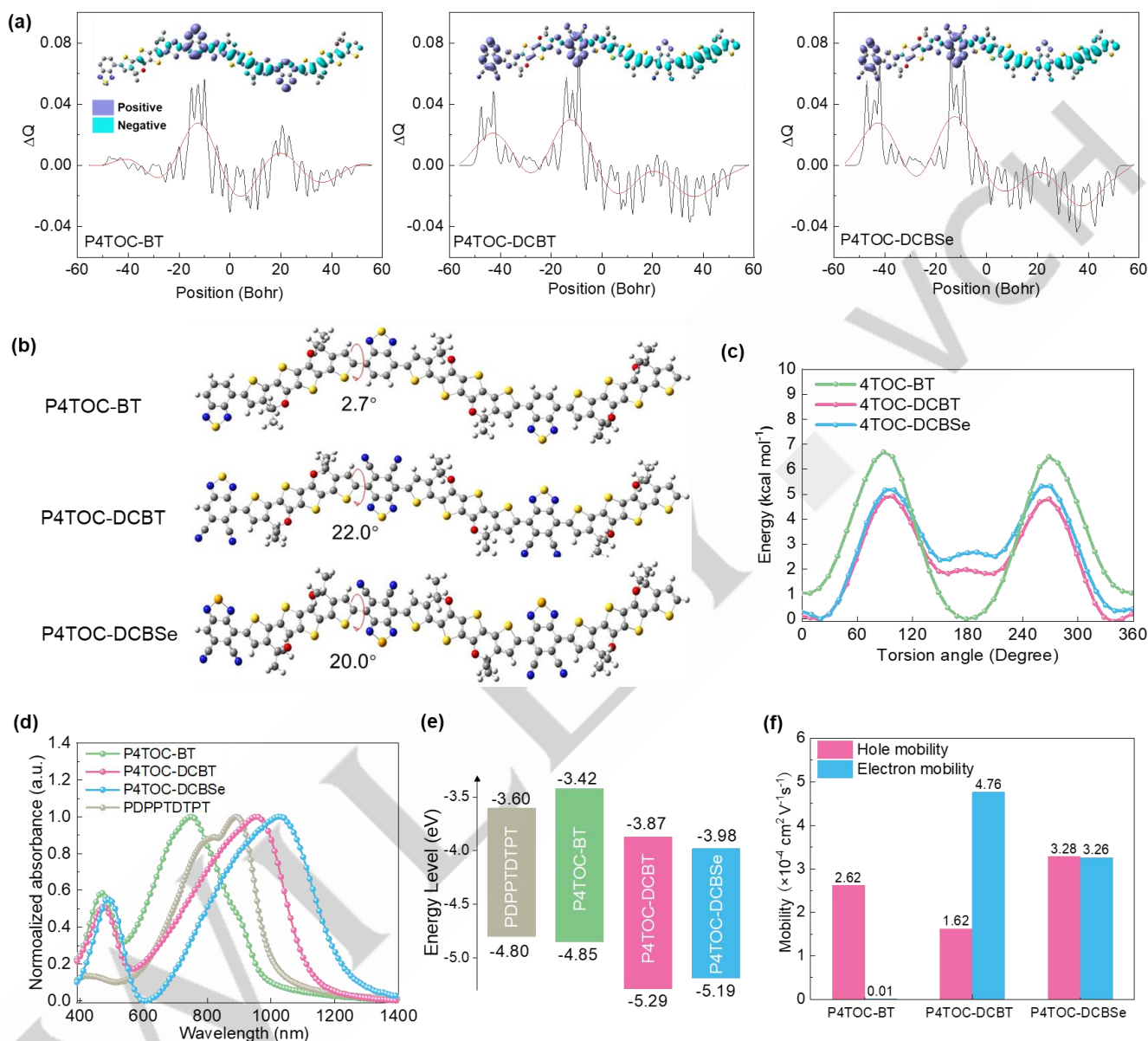

Figure 1. (a) Calculated FMO charge density difference ΔQ ($\Delta Q = \Psi^2_{LUMO} - \Psi^2_{HOMO}$) along the backbones of the polymers. (b) Optimized molecular geometries and (c) torsional energy surface scans of P4TOC-BT, P4TOC-DCBT and P4TOC-DCBSe. (d) Normalized UV−vis−NIR absorption spectra of the polymer films thermally annealed at 140 °C. (e) Diagram of HOMO and LUMO energy levels of the polymer donor and acceptors. (f) Charge mobilities of the neat polymer films obtained using single-carrier devices.

Table 1. Molecular weight, PDI and optical and electrochemical properties of P4TOC-BT, P4TOC-DCBT and P4TOC-DCBSe.

	M_n (kDa)/PDI	λ^{sol}_{max} (nm)	λ^{film}_{max} (nm)	E^{opt}_g (eV)	λ_{onset} (nm)	E_{HOMO} (eV)	E_{LUMO} (eV)
P4TOC-BT	17.5/1.43	736	751	1.24	996	-4.85	-3.42
P4TOC-DCBT	14.5/1.78	963	956	1.10	1132	-5.29	-3.87
P4TOC-DCBSe	16.2/1.47	1038	1033	0.99	1248	-5.19	-3.98

RESEARCH ARTICLE

Ultraviolet–visible–near infrared (UV-vis-NIR) absorption spectra of P4TOC-BT, P4TOC-DCBT and P4TOC-DCBSe in solution and film are shown in Figures S14 and 1d, respectively, and the relevant data are summarized in Table 1. Compared to P4TOC-BT with an absorption maximum (λ_{max}^{film}) at 751 nm, P4TOC-DCBT and P4TOC-DCBSe exhibit significantly redshifted absorption with λ_{max}^{film} at 956 and 1033 nm, respectively. The optical bandgaps (E_g^{opt}) calculated from the absorption onset of the films, are 1.24, 1.10 and 0.99 eV for P4TOC-BT, P4TOC-DCBT and P4TOC-DCBSe, respectively. In solution, all three polymers show temperature-dependent absorption spectra (Figure S15). The disaggregation temperature, at which the absorption peaks caused by aggregation disappear, for P4TOC-DCBT and P4TOC-DCBSe is 90 ℃, which is 40 ℃ higher than that of P4TOC-BT. The higher disaggregation temperature signifies stronger intermolecular interactions, which was attributed to the higher conformational stability of the CN substituted polymers. Cyclic voltammetry was conducted to estimate the FMO energy levels of the polymers. As depicted in Figure S16 and 1e, the HOMO/LUMO energy levels of P4TOC-BT, P4TOC-DCBT, and P4TOC-DCBSe are -4.85/-3.42, -5.29/-3.87 and -5.19/-3.98 eV, respectively. Therefore, the introduction of CN groups induced a greater downshift in LUMO levels than in HOMO levels, in accordance with the DFT calculations.

Charge transport properties of the polymers in neat films were evaluated through the space-charge-limited current (SCLC) method, as illustrated in Figures 1f and S17. Polymer P4TOC-BT is predominantly characterized by p-type transport with substantially higher hole mobility ($\mu_h = 2.62 \times 10^{-4}$ cm²/V·s) than electron mobility ($\mu_e = 1 \times 10^{-6}$ cm²/V·s), due to the high-lying FMOs. The introduction of electron-deficient CN groups profoundly improved the electron transport ability of the polymers. In the P4TOC-DCBT film, the μ_e reaches 4.76×10^{-4} cm²/V·s, much higher than its μ_h (1.62×10^{-4} cm²/V·s). P4TOC-DCBSe film shows nearly equivalent μ_h (3.28×10^{-4} cm²/V·s) and μ_e (3.26×10^{-4}

cm²/V·s), which could be derived from its relatively high-lying HOMO energy level. The high electron mobility as well as the low-lying LUMO levels indicate that the two CN substituted polymers have great potential as acceptor materials for OPDs.

Photodetection Performance of OPDs on Rigid Substrates

Given the wide bandgap and poor electron mobility of P4TOC-BT, we evaluated only the SWIR photodetection performance of P4TOC-DCBT and P4TOC-DCBSe using the device architecture of ITO/ZnO/PFN-Br/polymer donor:polymer acceptor/MoO₃/Ag. Polymer PDPPTDTPT (Figure S18), with FMOs (Figure 1e) well-matched to those of our acceptor materials, was selected as the donor material. The photodetection performance of the optimal OPDs is shown in Figure 2, and the detailed device data are listed in Tables 2 and S19. The optimal P4TOC-DCBSe-based device exhibits a response range of 400-1100 nm, with a maximum external quantum efficiency (EQE) of 14.2% at 960 nm (Figure 2a). The response range of the optimal P4TOC-DCBSe-based device extends to 1200 nm, beyond the response limit wavelength (~1100 nm) of the most widely used commercial Si-based photodetectors. Given that the absorption onset of PDPPTDTPT is around 1000 nm (Figure 1d), the response of the all-polymer OPDs beyond 1000 nm is originated from the polymer acceptors. Responsivity (R) is defined as the ratio of the photocurrent to the incident light intensity, and can be obtained as follows:

$$R = \frac{EQE \times \lambda}{100\% \times 1240} \quad (1)$$

where λ is the wavelength of incident light in nanometers. Compared to the P4TOC-DCBSe based devices, the P4TOC-DCBT-based device exhibits a higher R at 400-1080 nm, because of the higher EQE. In the wavelength range of 890-1010 nm, R reaches ~0.10 A/W for the P4TOC-DCBT-based device under zero bias, whereas for the P4TOC-DCBSe-based device, the maximum R is 0.06 A/W at 880 nm (Figure 2b).
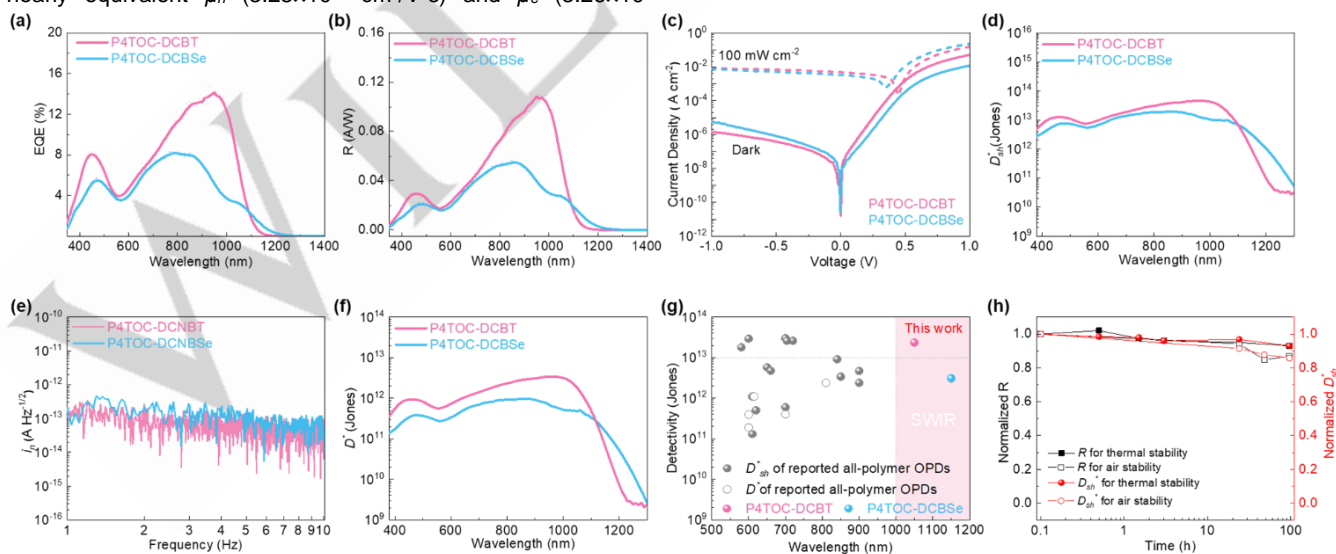

Figure 2. (a) EQE and (b) R of the all-polymer OPDs under zero bias. (c) J-V curves measured in the dark and under AM 1.5G irradiation (100 mW cm⁻²). (d) D_{sh}^* of the OPDs under zero bias. (e) Noise current spectra under zero bias. (f) D^* of the OPDs under zero bias. (g) Plot of specific detectivity versus wavelength for the all-polymer OPDs reported in the literature[50-70] (Table S1) and this work. (h) Normalized R and D_{sh}^* at 1050 nm as functions of storage time for P4TOC-DCBT-based OPDs under heating at 60℃ or exposing in air without encapsulation.

5

RESEARCH ARTICLE

Table 2. Performance parameters of P4TOC-DCBT and P4TOC-DCBSe based all-polymer OPDs under zero bias.

Acceptor	$R^{[a]}$(A/W)	$D_{sh}^{*[a]}$/Jones	$D^{*[a]}$/Jones	$D_{sh}^{*[b]}$/Jones	$D^{*[b]}$/Jones	Response time/µs
P4TOC-DCBT	0.11	$4.73×10^{13}$	$3.53×10^{12}$	$2.37×10^{13}$	$1.77×10^{12}$	1.36
P4TOC-DCBSe	0.06	$1.96×10^{13}$	$9.80×10^{11}$	$9.48×10^{12}$	$4.75×10^{11}$	2.38

[a] The maximum R or specific detectivity observed at 960 nm for the P4TOC-DCBT based device and 880 nm for the P4TOC-DCBSe based device. [b] The specific detectivity of the OPDs at 1050 nm.

Specific detectivity is a key figure-of-merit for quantifying the ability of a photodetector to detect weak light signals. Assuming that the shot noise dominates the total noise, the shot-noise-limited specific detectivity (D_{sh}^*) can be calculated as

$$D_{sh}^* = \frac{R}{\sqrt{2qJ_d}} \quad (2)$$

where J_d and q represent the dark current and the elementary charge, respectively. As depicted in Figure 2c, both P4TOC-DCBT and P4TOC-DCBSe based devices exhibit relatively low J_d values, $1.7×10^{-11}$ and $2.5×10^{-11}$ A/cm^2, respectively, under zero bias. Owing to their low J_d, the P4TOC-DCBT-based detector shows D_{sh}^* of over 10^{13} Jones from 610 to 1080 nm under zero bias. The P4TOC-DCBSe-based detector exhibits D_{sh}^* of over 10^{12} Jones from 400 to 1200 nm under zero bias (Figure 2d). These results mean the all-polymer OPDs are able to operate efficiently without the need for an external power supply to provide bias, which is known as self-powered operation. To precisely evaluate the detectivity of the photodetectors, the total noise current (i_n), including the shot, thermal, and flicker noises, was measured using an electrometer by Fourier transform analysis, and the specific detectivity (D^*) was calculated as

$$D^* = \frac{R\sqrt{AB}}{i_n} \quad (3)$$

where A is the device area (0.038 cm^2 in this work), B is the measurement bandwidth, and i_n is the total noise current. As shown in Figure 2e, the device based on P4TOC-DCBT exhibits i_n of $6.1×10^{-15}$ A Hz$^{-1/2}$ at 10 Hz, which is considerably lower than that of the P4TOC-DCBSe-based device ($1.1×10^{-14}$ A Hz$^{-1/2}$ at 10 Hz). As a result, the device based on P4TOC-DCBT shows a higher D^* within 300-1100 nm than the P4TOC-DCBSe-based device. The D^* of the P4TOC-DCBT-based device exceeds 10^{12} Jones at 650 -1070 nm and reaches $3.0×10^{12}$ Jones at 890-1010 nm (Figure 2f), which is comparable to the performance of commercially available inorganic photodetectors. The performance of reported all-polymer OPDs and SWIR OPDs based on polymer donor:fullerene or SMA is summarized in Figure 2g and Tables S1 and S2. The high specific detectivity

makes P4TOC-DCBT-based all-polymer OPDs rank in the top tier of the reported OPDs and the best SWIR all-polymer OPDs in photovoltaic mode.

Reverse bias (−0.1, −0.5 and −1 V) was used to improve the charge-carrier extraction efficiency in OPDs (Figure S20, and Table S3 in SI). Compared to the devices under zero bias, the devices based on both P4TOC-DCBT and P4TOC-DCBSe present higher EQE and R in the whole photoresponse region upon reverse bias. The maximum EQE and R values reach 27.9% and 0.21 A W$^{−1}$ at 940 nm for the P4TOC-DCBT-based devices, and 16.0% and 0.11 A W$^{−1}$ at 880 nm for the P4TOC-DCBSe-based devices under −1 V. However, under the reverse bias, J_d values of the OPDs sharply increase, and the J_d of the P4TOC-DCBSe-based device increased faster than that of the P4TOC-DCBT-based device. As a result, D_{sh}^* values of the OPDs based on P4TOC-DCBT and P4TOC-DCBSe upon reverse bias are much lower than those upon zero bias. The maximum D_{sh}^* values of the P4TOC-DCBT-based devices are $1.13×10^{12}$, $4.67×10^{11}$ and $3.16×10^{11}$ Jones (at 940 nm) under the bias of -0.1, -0.5 and -1 V, respectively, which are higher than those of the P4TOC-DCBSe-based devices ($5.07×10^{11}$, $1.95×10^{11}$ and $8.92×10^{10}$ Jones at 880 nm).

The stability of the P4TOC-DCBT based OPDs was assessed upon continuous heating and in air without encapsulation. As shown in Figures 2h, S21 and S22, the devices retain ~93% of their initial R and D_{sh}^* at 1050 nm after continuous heating at 60 ℃ for 96 h in an argon atmosphere. The excellent thermal stability of the photodetectors should be derived from the stable morphology of the all-polymer blend films. Additionally, the unencapsulated all-polymer OPDs exhibit satisfactory stability in air (Figure 2h). After exposure to air for 96 h, R and D_{sh}^* at 1050 nm are ~86% of the initial values, indicating the good stability of the polymer semiconductors. The long-term stability of the SWIR OPDs can ensure the reliability and durability of the photodetectors.
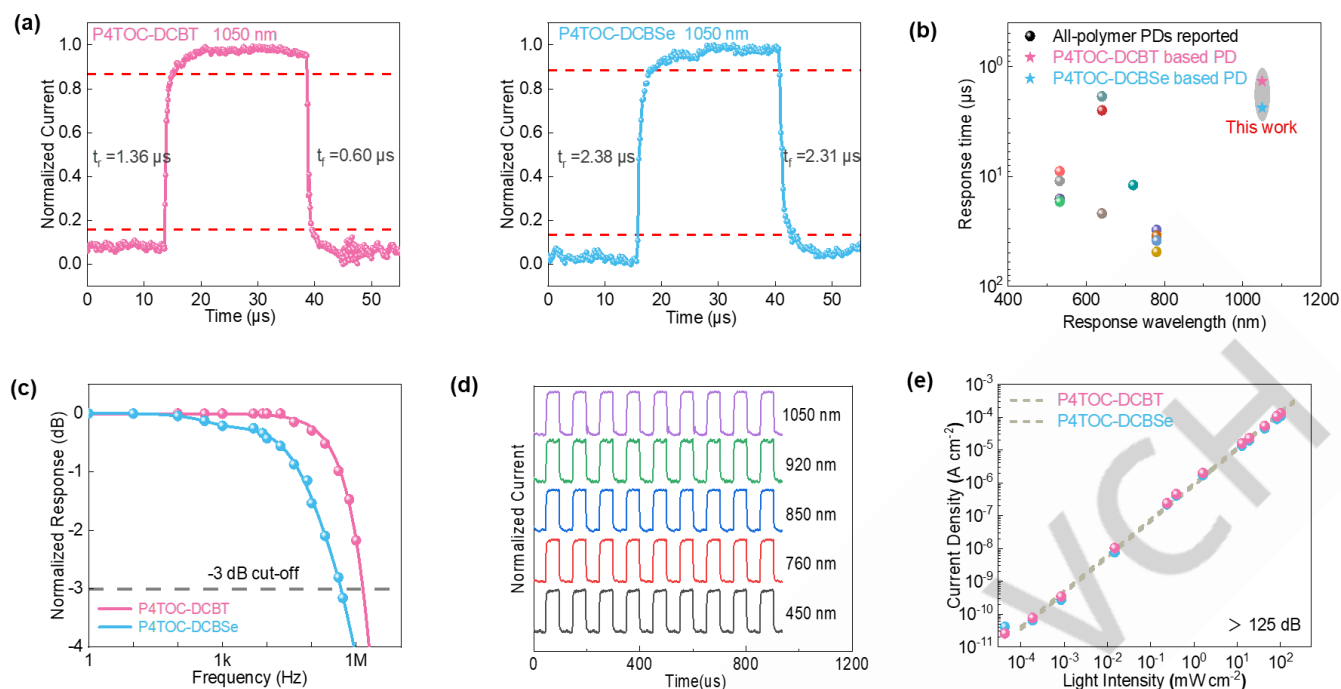
6

RESEARCH ARTICLE

Figure 3. (a) Photo transient response of the OPDs under a light modulation frequency of 40 kHz. (b) Statistical graph of response time versus wavelength for all-polymer photodetectors reported in the literature[58, 60, 64, 68, 70-73] (Table S4) and this work. (c) The -3 dB cutoff frequency of the OPDs at 1050 nm. (d) Photo transient response of the OPDs at different wavelengths. (e) LDR of the OPDs at 1050 nm.

We also investigated the response time, -3 dB cutoff frequency (f_{-3dB}), and linear dynamic range (LDR) of the OPDs under SWIR light irradiation, which can reflect the capability of photodetectors to accurately detect and process complex and rapidly changing optical signals. The OPDs were tested under the 1050 nm light-emitting diode (LED) illumination controlled by a signal generator. The measured rise time (t_r) and fall time (t_f) are determined based on the time it takes for the output signal to rise from 10% to 90% and to fall from 90% to 10% after the light signal is applied. As illustrated in Figure 3a, the t_r/t_f values are 1.36/0.60 μs for P4TOC-DCBT based device, and 2.38/2.31 μs for the P4TOC-DCBSe-based device under zero bias. To the best of our knowledge, the response time of the P4TOC-DCBT-based photodetector is the shortest among all-polymer photodetectors reported thus far (Figure 3b), suggesting its superior capability in handling transient photo-signals. The -3 dB cutoff frequency indicates the maximum frequency at which the device can operate effectively without substantial loss in signal power. As shown in Figure 3c, the f_{-3dB} values were found to be 1.5 and 0.46 MHz for P4TOC-DCBT- and P4TOC-DCBSe- based devices, respectively. The faster photo-response of the P4TOC-DCBT-based self-powered OPDs demonstrates their considerable potential in medical monitoring, optical communication and imaging. Additionally, the P4TOC-DCBT-based device maintains good transient photo-response when exposed to square-wave signals of different wavelengths within the spectral detection range (Figure 3d).

LDR refers to the region where the electrical output of a photodetector remains linear with light intensity. LDR can be calculated from

$$LDR = 20log\frac{J_{max}}{J_{min}} \quad (7)$$

where J_{max} represents the photocurrent at the onset of saturation, indicating the upper limit of linearity, and J_{min} denotes the minimum detectable photocurrent within the linear region, corresponding to the weakest signal the detector is capable of accurately identifying. Figure 3e presents the LDR of the two devices under 1050nm illumination. Benefiting from their low dark current, both P4TOC-DCBT- and P4TOC-DCBSe-based detectors exhibit an LDR exceeding 125 dB (the LDR values are underestimated because of the upper load power limit of the 1050-nm LED lamp used), rivalling InGaAs photodetectors (132 dB)[74]. The results indicate that these self-powered OPDs maintain a high-fidelity signal detection over a wide range of light intensities.

Charge Generation, Trap States, and Analysis of Dark current

Photoluminescence (PL) quenching efficiency of the polymer acceptors in blend films was investigated to gain insights into the impact of exciton dissociation on SWIR photodetection. The PL spectra of the neat polymer films and the blend films are illustrated in Figure 4a. For both PDPPTDTPT:P4TOC-DCBT and PDPPTDTPT:P4TOC-DCBSe blend films, the fluorescence from PDPPTDTPT was quenched efficiently, indicating efficient electron transfer from PDPPTDTPT to the acceptor. However, the fluorescence of both acceptors in the blend films is not completely quenched. The fluorescence quenching efficiency of the acceptor is 82.3 % for the PDPPTDTPT:P4TOC-DCBT film and 72.3 % for the PDPPTDTPT:P4TOC-DCBSe blend film. The higher quenching efficiency of the fluorenscence from the acceptor

7

RESEARCH ARTICLE

indicates the more efficient dissociation of the excitons generated by the acceptor in the PDPPTDTPT:P4TOC-DCBT blend film. Given that both blend films show nanoscale phase separation (as discussed below), the less efficient fluorescence quenching of PDPPTDTPT:P4TOC-DCBSe blend could be mainly ascribed to the smaller HOMO offset between PDPPTDTPT and P4TOC-DCBSe, which cannot provide enough driving force for the dissociation of the excitons generated by the acceptor. The results is consistent with the lower EQE of the P4TOC-DCBSe -based devices in SWIR region compared to the visible light region. The more efficient charge separation and collection in the PDPPTDTPT-based OPDs was also verified by the higher ratio of

photocurrent density (J_{ph})/saturation current density (J_{sat}) according to the J_{ph} versus effective voltage (V_{eff}) plot (Figure 4b). Carrier mobility of the blend films was also measured by the SCLC method (Figures S23 and 4c). Compared to the PDPPTDTPT:P4TOC-DCBSe film (μ_h = 8.8×10^{-5} cm²/V·s, μ_e = 6.5×10^{-5} cm²/V·s), the PDPPTDTPT:P4TOC-DCBT film exhibits higher μ_h and μ_e (1.3×10^{-4} cm²/V·s and 7.6×10^{-5} cm²/V·s, respectively), which was attributed to the higher μ_e of neat P4TOC-DCBT and a more distinct phase separation in the blend film (Figure S24). The higher EQE and R of the P4TOC-DCBT-based OPDs were explained by their more efficient exciton dissociation and charge transport.
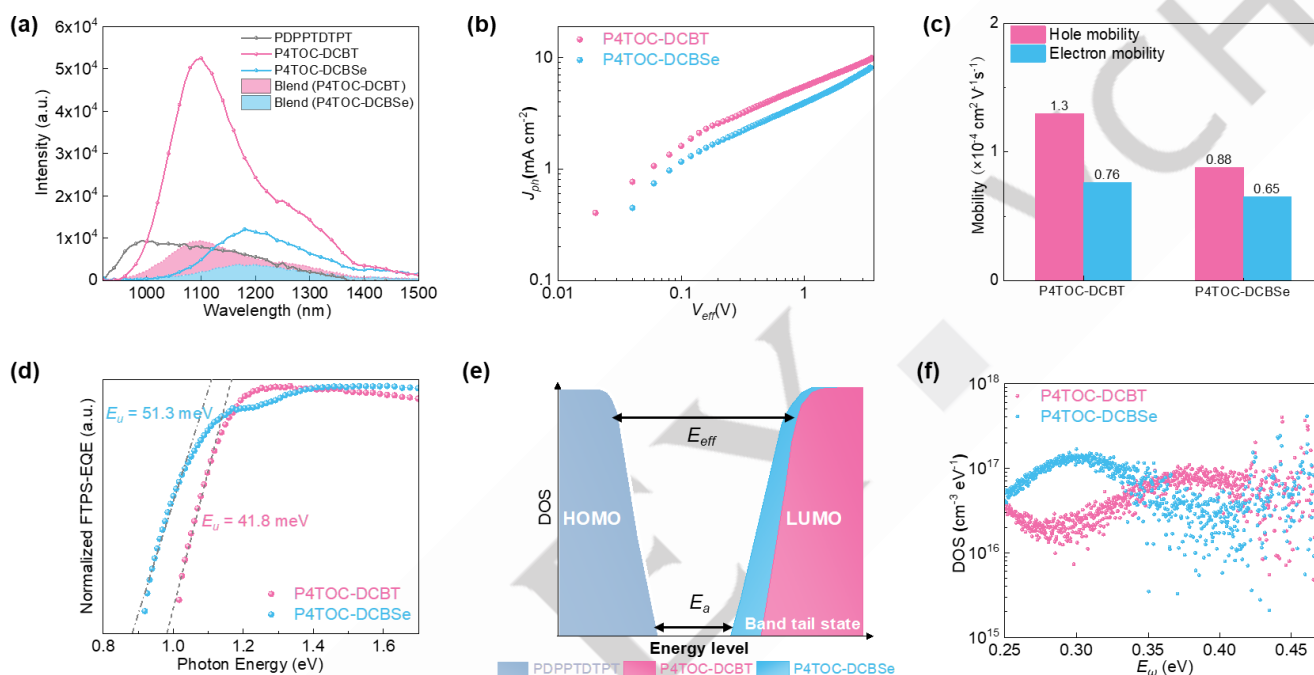

Figure 4. (a) Fluorescence spectra of the neat polymer films and blend films excited at 900 nm. (b) $J_{ph}-V_{eff}$ curves of the P4TOC-DCBT- and P4TOC-DCBSe-based OPDs, with J_{ph}/J_{sat} of 64% and 51%, respectively, under short-circuit conditions. The J_{ph} values obtained at V_{eff} of 3.5 V are considered as pseudo saturation current density. (c) Charge mobility of the blend films obtained from SCLC method. (d) Normalized FTPS-EQE spectra of the OPDs. (e) Diagram of thermal activation energy, effective energy and band tail state. (f) Trap DOS for the OPDs.

The width of the electronic density of states (DOS) distribution reflects the extent of the energetic disorder, which was quantitatively characterized by the Urbach energy (E_u) through evaluating the tail state of the Fourier-transform photocurrent spectroscopy EQE (FTPS-EQE). As shown in Figure 4d, E_u is 41.8 meV for the P4TOC-DCBT based device, and 51.3 meV for the P4TOC-DCBSe based device. This indicates the lower extent of energetic disorder in the P4TOC-DCBT-based detector and a smaller extension of the band-tail states into the bandgap. Recent studies have demonstrated that the thermal activation energy (E_a) of J_d generation is closely related to E_{eff} (defined as the difference between the HOMO level of the donor and the LUMO level of the acceptor) and band-tail state (Figure 4e).[75-77] Because the same donor was used, the shallow LUMO of P4TOC-DCBT means the larger E_{eff} of PDPPTDTPT:P4TOC-DCBT blend in comparison to PDPPTDTPT:P4TOC-DCBSe blend. The larger E_{eff} and smaller

E_u of the PDPPTDTPT:P4TOC-DCBT-based device compared to those of the PDPPTDTPT:P4TOC-DCBSe-based device are favorable for increasing E_a, which can significantly suppress the thermal generation of J_d.

To further reveal the trap density of state distribution, we carried out the capacitance–frequency ($C-\omega$) measurements to characterize the trap density at different energy level depths. Trap DOS distribution can be extracted from following equations:

$$\text{DOS}(E_\omega) = -\frac{V_{bi}}{qAW}\frac{\omega}{kT}\frac{dC}{d\omega} \quad (10)$$

$$E_\omega = kT\ln\left(\frac{\omega_0}{\omega}\right) \quad (11)$$

where E_ω is the trap energy, V_{bi} is the built-in potential (voltage at the intersection of J-V curves under illumination and in the dark; Figure S25), W is depletion width (100 nm is used), ω is the angular frequency, ω_0 is the attempt-to-escape frequency and C is the capacitance. The C–ω curves and the corresponding trap DOS are depicted in Figures S26 and 4f, respectively. In the

8

RESEARCH ARTICLE

shallow energy level region, the trap density of the device based on P4TOC-DCBT is significantly lower than that of the device based on P4TOC-DCBSe, which is conducive to efficient carrier transport and collection. In the deep energy level region, P4TOC-DCBT- and P4TOC-DCBSe-based devices exhibit a similar DOSs, indicating the analogous types and distributions of defects.[78-79] Subsequently, we adopted a single Gaussian distribution model to fit the DOS data, extracting the trap DOS (N_t), trap energy (E_t) and Gaussian width (σ). As listed in Table S5, the P4TOC-DCBT- and P4TOC-DCBSe-based devices showed the DOS for deep traps (N_t) of 1.59×10^{15} and 1.93×10^{15} cm^{-3}, aligning with the lower J_d and the faster photo-response of the P4TOC-DCBT-based device.

The high J_d of the OPDs upon reverse bias stems from severe carrier injection from the electrodes into the active layers.[80] Due to the deeper LUMO energy level of P4TOC-DCBSe compared to P4TOC-DCBT, the electron injection barrier of the P4TOC-DCBSe-based devices is lower. Therefore, under reverse bias, the increase in J_d of the P4TOC-DCBSe-based devices is greater than that of the P4TOC-DCBT-based devices. In theory, the J_d under reverse bias for the all-polymer OPDs can be further suppressed by introduction of suitable interface layers with better electron (or hole) blocking effect between the anode (or cathode) and the active layers.

Film Morphology, Mechanical Properties of the Films and Performance of the Flexible OPDs

The film morphology was investigated using atomic force microscopy (AFM), and transmission electron microscopy (TEM). As shown in Figure S24a, both PDPPTDTPT:P4TOC-DCBT and PDPPTDTPT:P4TOC-DCBSe blend films display smooth surface with low root-mean-square roughness of 1.35 and 1.20 nm,

respectively. The short-fiber-like structure is observed for PDPPTDTPT:P4TOC-DCBT blend film, while PDPPTDTPT:P4TOC-DCBSe film presents homogeneous morphology. The TEM images (Figure S24b) exhibit similar characteristics to AFM. Both blend films show nanoscale phase separation, allowing excitons to efficiently diffuse to the interface between the donor and acceptor. Compared to PDPPTDTPT:P4TOC-DCBSe blend film, PDPPTDTPT:P4TOC-DCBT film shows more distinct phase separation, which is beneficial for charge transport. The molecular order of the all-polymer blend films was studied using X-ray diffraction (XRD). As illustrated in Figure 5a, no discernible diffraction peaks are observed in the in-plane direction for both blend films. At the same time, in the out-of-plane direction, weak (100) diffraction peaks are observed for the two blend films. The low molecular order is less susceptible to formation of micro-cracks and stress concentration, which should be beneficial for achieving high flexibility and stretchability. [81-82] The low crystallinity of the blend films should be ascribed to the nearly amorphous character of P4TOC-DCBT and P4TOC-DCBSe, as revealed by the XRD patterns of the neat films (Figure S27).

Thin-film tensile properties of the blend and neat films were investigated through the film-on-elastomer (FOE) approach with polydimethylsiloxane (PDMS) as the elastic substrate. As shown in Figure S28, no cracks are observed in the PDPPTDTPT neat films as strains up to 150%. The crack onset strain (COS) values of P4TOC-DCBT and P4TOC-DCBSe neat films are ~15%. The lower molecular weights of the polymer acceptors should be responsible for the COS values of these films being lower than that of PDPPTDTPT. The COS values are ~30% for the PDPPTDTPT:P4TOC-DCBT and PDPPTDTPT:P4TOC-DCBSe blend films (Figure 5b), higher than those of most polymer:small molecule films.
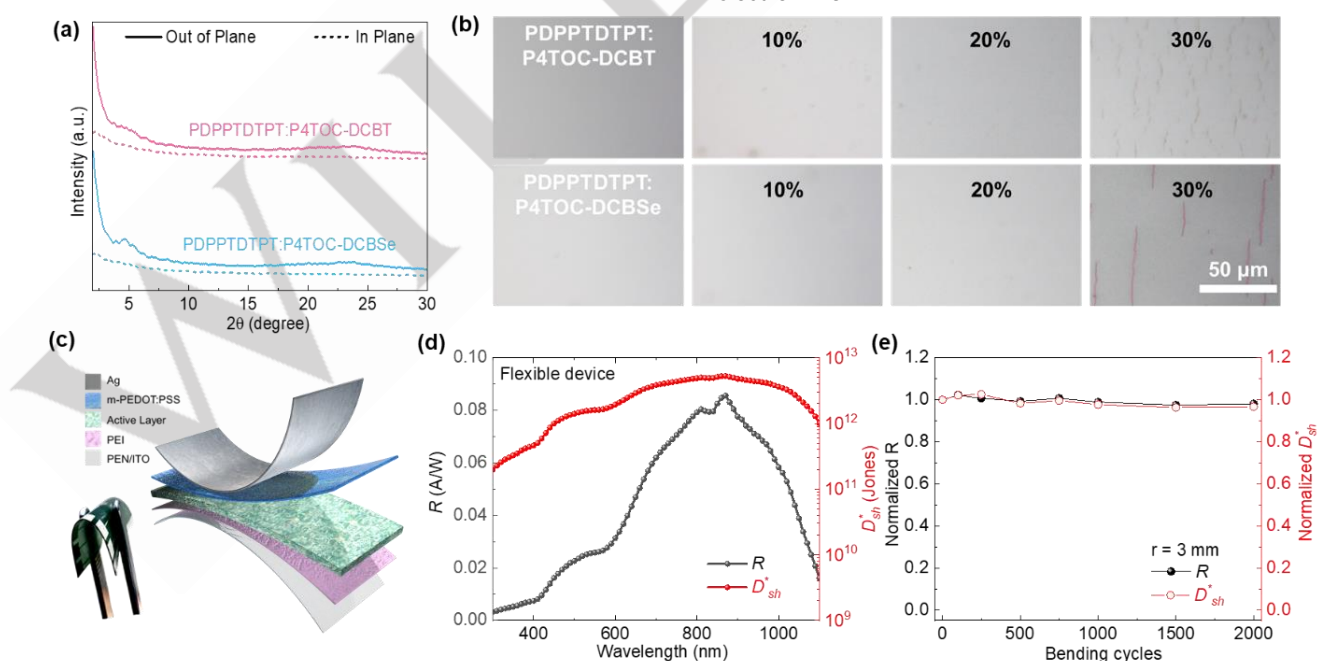

Figure 5. (a) XRD patterns of the PDPPTDTPT:P4TOC-DCBT and PDPPTDTPT:P4TOC-DCBSe blend films. (b) Polarized optical microscopy (POM) images of the blend films under different strain values. (c) Schematic of the flexible photodetector. (d) R and D_{sh}^* of the P4TOC-DCBT-based flexible OPDs at zero bias. (e) Normalized R and D_{sh}^* at 1050 nm as functions of the blending cycles of the flexible OPDs.

9

RESEARCH ARTICLE

We further used PDPPTDTPT:P4TOC-DCBT to fabricate flexible OPDs with a device architecture of ITO/PEI/polymer donor:polymer acceptor/m-PEDOT:PSS/Ag (Figure 5c). The flexible OPDs exhibitan increase in the dark current compared to the rigid ITO-based OPDs, primarily due to the low shunt resistance caused by the interfaces. As shown in Figure 5d, D_{sh}^* of the flexible OPDs at zero bias exceeds 10^{12} Jones in the spectral range from 460 to 1090 nm. The maximum R of 0.08 A/W and D_{sh}^* of 5.29×10^{12} Jones were achieved at 870 nm. Following this, the flexible OPDs were subjected to bending tests with a bending radius of 3 mm to evaluate their mechanical stability. As depicted in Figure 5e, after 2000 cycles of bending to a 3 mm radius, the flexible OPDs show a small reduction in R (< 2%) and D_{sh}^* (< 4%). Owing to the poor mechanical durability of the ultra-thin PEI layer (thickness of ~2 nm) and the interfacial loss, it is expected that the detectivity and bending properties of the flexible all-polymer OPDs may be improved through interface engineering.

Applications of all-polymer SWIR OPDs

To demonstrate the potential application of the flexible all-polymer SWIR OPDs based on P4TOC-DCBT, we conducted photoplethysmography (PPG) measurements under illumination of 1050 nm LED. Due to the changes in vascular volume during the cardiac cycle, light intensity penetrating the tested body part (a finger in this test) exhibits periodic changes, which can be converted into electrical signals by OPDs for health monitoring. SWIR light shows greater penetration depth in biological tissues than visible light, allowing for reliable PPG signal detection. As

illustrated in Figure 6a, P4TOC-DCBT-based flexible SWIR OPDs adhered to the fingers show clear PPG signals. The heart rates of a volunteer calculated from the PPG results are 90 and 120 beats per minute before and after exercise, respectively, consistent with the medical measurements.

Owing to sensitive and rapid response, P4TOC-DCBT-based flexible OPDs were tested for application in optical communication, which allows high-speed and large-capacity data transmission without external electromagnetic interference and safety issues. As illustrated in Figure 6b, the text is inputted on a computer, and converted into ASCII code. Then, the LED lamp is modulated by a serial communication module to send optical signals according to the ASCII code. The P4TOC-DCBT-based OPD receives the signals and outputs electrical signals, which are further converted into ASCII code by the serial communication module. Finally, the text is shown on the display screen. When we inputted the text 'TJU' on the computer, the same text was displayed on the screen and the output signal of the P4TOC-DCBT-based OPD kept pace with the input signal.

The OPD based on P4TOC-DCBT was also used for single-pixel SWIR imaging at a wavelength of 1050 nm. A stainless stencil masks with the hollow letter patterns of 'T', 'J' and 'U' were moved along the x- and y-axes. During illumination, the incident light only passed through the hollow areas, and was detected by the OPDs. The images were obtained by plotting a heatmap of the photocurrent. As shown in Figure 6c, the images exhibited well-defined boundaries, with the original appearance of the letters being accurately replicated.
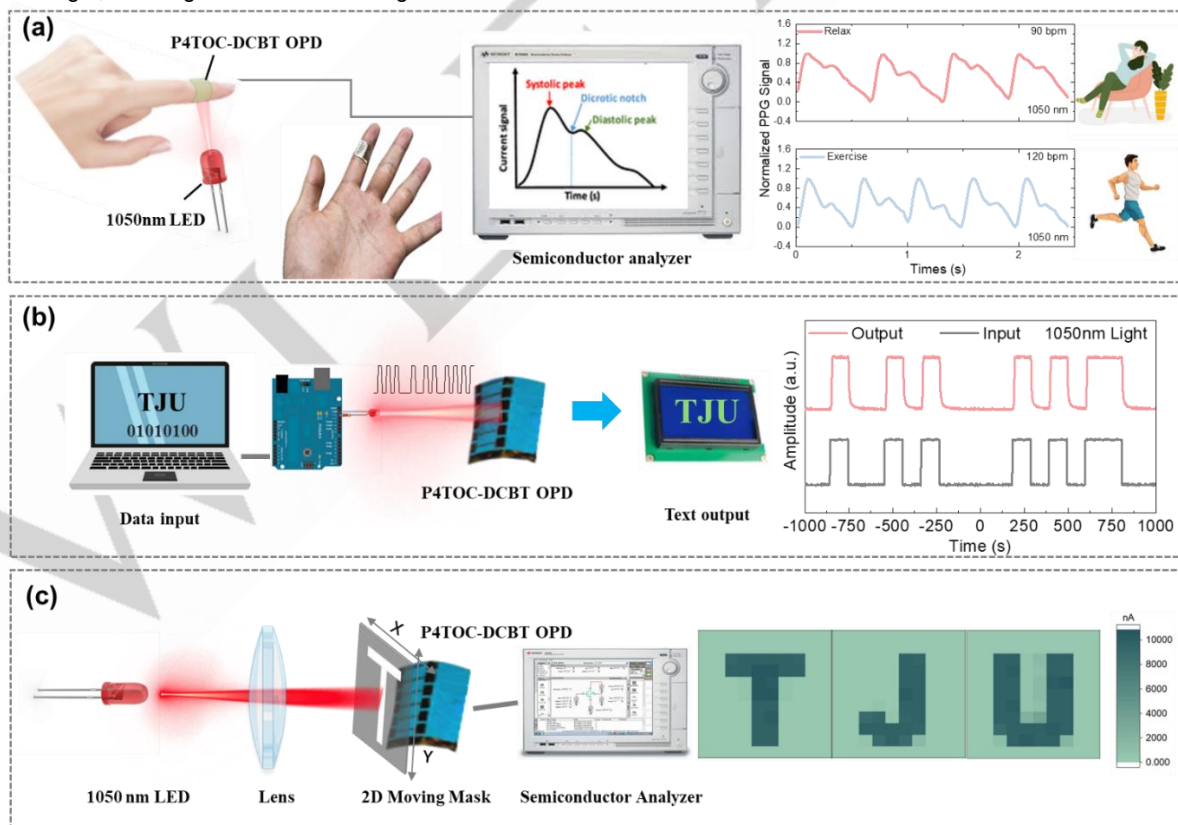

Figure 6. (a) Schematic diagram for heart rate monitoring, and PPG signals detected by P4TOC-DCBT based OPD at 1050 nm. (b) Schematic diagram of optical communication, including input and output signals at 1050 nm. (c) Schematic diagram of SWIR imaging and the captured image under illumination at 1050 nm.

10

RESEARCH ARTICLE

Conclusion

We used strong electron-withdrawing DCBT and DCBSe as acceptor units and fused-ring 4TOC as a donor unit to construct polymer acceptors with ultra-NBG, low-lying LUMO levels and high electron mobility. The rigid structure and stable conformation of the polymers are proved favorable for suppressing energetic disorder and reducing trap density, thereby achieving sensitive photodetection. Benefiting from the narrower bandgap, P4TOC-DCBSe-based all-polymer OPDs show broad photo-response extending to 1200 nm beyond the response range of Si-based detectors. The device based on P4TOC-DCBT exhibits higher EQE and R than the P4TOC-DCBSe-based device because of more efficient exciton dissociation and charge transport, and lower J_d because of lower E_{eff}, E_u and trap DOS. Consequently, P4TOC-DCBT-based devices achieved high D_{sh}^* and D^* over 10^{13} and 10^{12} Jones in the SWIR region, respectively, along with a short response time of 1.36 μs. These results make the P4TOC-DCBT-based device the best-performing all-polymer OPD reported thus far for SWIR photodetection in photovoltaic mode. The all-polymer OPDs also exhibited excellent thermal and air stabilities owing to inhibited molecular diffusion and good chemical stability of the polymers. Moreover, the all-polymer blend films present desirable stretchability, and the flexible devices exhibit D_{sh}^* over 10^{12} Jones from 1000 to 1100 nm, and maintain over 98% of the initial R after 2000 bending cycles. This study demonstrates the significance of developing ultra-NBG polymer acceptors in gaining all-polymer OPDs with sensitive SWIR photodetection and showcases great application potential of the all-polymer blend systems in next-generation wearable photodetection technologies.

Acknowledgements

[1] Z. Wu, Y. Zhai, H. Kim, J. D. Azoulay, T. N. Ng, *Accounts of Chemical Research* **2018**, 51, 3144.

[2] E. Hemmer, A. Benayas, F. Légaré, F. Vetrone, *Nanoscale horizons* **2016**, 1, 168.

[3] L. A. Sordillo, Y. Pu, S. Pratavieira, Y. Budansky, R. R. Alfano, *Journal of biomedical optics* **2014**, 19, 056004.

[4] Z. Lan, M.-H. Lee, F. Zhu, *Advanced Intelligent Systems* **2022**, 4, 2100167.

[5] H. M. Luong, C. Kaiyasuan, A. Yi, S. Chae, B. M. Kim, P. Panoy, H. J. Kim, V. Promarak, Y. Miyata, H. Nakayama, *ACS Energy Letters* **2024**, 9, 1446.

[6] Y. Chen, Y. Zheng, J. Wang, X. Zhao, G. Liu, Y. Lin, Y. Yang, L. Wang, Z. Tang, Y. Wang, *Science Advances* **2024**, 10, eadm9631.

[7] M. Yang, B. Yin, G. Hu, Y. Cao, S. Lu, Y. Chen, Y. He, X. Yang, B. Huang, J. Li, *Chem* **2024**, 10, 1425.

[8] T. Li, G. Hu, L. Tao, J. Jiang, J. Xin, Y. Li, W. Ma, L. Shen, Y. Fang, Y. Lin, *Science Advances* **2023**, 9, eadf6152.

[9] Y.-C. Huang, T.-Y. Wang, Z.-H. Huang, S. R. M. S. Santiago, *ACS Applied Materials & Interfaces* **2024**.

[10] N. Li, Z. Lan, Y. S. Lau, J. Xie, D. Zhao, F. Zhu, *Advanced Science* **2020**, 7, 2000444.

[11] B. Yin, X. Zhou, Y. Li, G. Hu, W. Wei, M. Yang, S. Jeong, W. Deng, B. Wu, Y. Cao, *Advanced Materials* **2024**, 36, 2310811.

[12] B.-H. Jiang, F.-C. Hsiao, Y.-R. Lin, C.-H. Lin, Y. A. Shen, Y.-Y. Hsu, P.-H. Lee, Y.-W. Su, H.-R. Lu, C.-W. Lin, *ACS Applied Materials & Interfaces* **2023**, 15, 10907.

[13] J. Yang, J. Huang, R. Li, H. Li, B. Sun, Q. Lin, M. Wang, Z. Ma, K. Vandewal, Z. Tang, *Chemistry of Materials* **2021**, 33, 5147.

[14] Y. Zheng, Y. Chen, X. Zhu, *Acta Polymerica Sinica* **2022**, 53, 354.

[15] T. Kim, J.-H. Kim, T. E. Kang, C. Lee, H. Kang, M. Shin, C. Wang, B. Ma, U. Jeong, T.-S. Kim, *Nature Communications* **2015**, 6, 8547.

[16] Y. Wu, Y. Yuan, D. Sorbelli, C. Cheng, L. Michalek, H.-W. Cheng, V. Jindal, S. Zhang, G. LeCroy, E. D. Gomez, *Nature communications* **2024**, 15, 2170.

[17] H. Kang, W. Lee, J. Oh, T. Kim, C. Lee, B. J. Kim, *Accounts of chemical research* **2016**, 49, 2424.

[18] S. Sahu, K. Tripathy, M. Bhattacharjee, D. Chopra, *Chemical Communications* **2024**, 60, 4382.

[19] Y. Lin, J. Wang, Z. G. Zhang, H. Bai, Y. Li, D. Zhu, X. Zhan, *Advanced Materials* **2015**, 27, 1170.

[20] J. Yuan, Y. Zhang, L. Zhou, G. Zhang, H.-L. Yip, T.-K. Lau, X. Lu, C. Zhu, H. Peng, P. A. Johnson, *Joule* **2019**, 3, 1140.

[21] Z. Zheng, J. Wang, P. Bi, J. Ren, Y. Wang, Y. Yang, X. Liu, S. Zhang, J. Hou, *Joule* **2022**, 6, 171.

[22] Q. Nie, A. Tang, Q. Guo, E. Zhou, *Nano Energy* **2021**, 87, 106174.

[23] Q. He, P. Ufimkin, F. Aniés, X. Hu, P. Kafourou, M. Rimmele, C. L. Rapley, B. Ding, *SusMat* **2022**, 2, 591.

[24] D. Li, H. Wang, J. Chen, Q. Wu, *Chemistry–A European Journal* **2024**, 30, e202303155.

[25] J. Du, M. C. Biewer, M. C. Stefan, *Journal of Materials Chemistry A* **2016**, 4, 15771.

[26] Y. Wang, T. Michinobu, *Journal of Materials Chemistry C* **2016**, 4, 6200.

[27] Z. Liang, J. He, B. Zhao, Y. Chen, L. Ye, M. Li, Y. Geng, *Science China Chemistry* **2023**, 66, 216.

[28] S. Liang, J. Xu, Y. Xu, W. Ni, M. Li, Y. Geng, *Dyes and Pigments* **2024**, 228, 112226.

[29] A. Casey, S. D. Dimitrov, P. Shakya-Tuladhar, Z. Fei, M. Nguyen, Y. Han, T. D. Anthopoulos, J. R. Durrant, M. Heeney, *Chemistry of Materials* **2016**, 28, 5110.

[30] S. Shi, H. Wang, P. Chen, M. A. Uddin, Y. Wang, Y. Tang, H. Guo, X. Cheng, S. Zhang, H. Y. Woo, *Polymer Chemistry* **2018**, 9, 3873.

[31] K. Feng, J. Huang, X. Zhang, Z. Wu, S. Shi, L. Thomsen, Y. Tian, H. Y. Woo, C. R. McNeill, X. Guo, *Advanced Materials* **2020**, 32, 2001476.

[32] J. Lu, J. Yuan, W. Guo, X. Huang, Z. Liu, H. Zhao, H.-Q. Wang, W. Ma, *Polymer Chemistry* **2014**, 5, 4772.

[33] H. S. Kim, T. H. Lee, J. Yeop, H. W. Cho, J. W. Kim, S. Y. Park, J. B. Park, J. Y. Kim, D.-H. Hwang, *The Journal of Physical Chemistry C* **2018**, 122, 16613.

[34] B. Schweda, M. Reinfelds, P. Hofstadler, G. Trimmel, T. Rath, *ACS Applied Energy Materials* **2021**, 4, 11899.

[35] S. Dey, *Small* **2019**, 15, 1900134.

[36] J. Wang, X. Zhan, *Accounts of Chemical Research* **2020**, 54, 132.

[37] J. Wang, P. Xue, Y. Jiang, Y. Huo, X. Zhan, *Nature Reviews Chemistry* **2022**, 6, 614.

[38] J. Wang, Y. Xie, K. Chen, H. Wu, J. M. Hodgkiss, X. Zhan, *Nature Reviews Physics* **2024**, 1.

[39] T. Li, H. Zhang, Z. Xiao, J. J. Rech, H. Niu, W. You, L. Ding, *Materials Chemistry Frontiers* **2018**, 2, 700.

[40] Z. Xiao, S. Yang, Z. Yang, J. Yang, H. L. Yip, F. Zhang, F. He, T. Wang, J. Wang, Y. Yuan, *Advanced Materials* **2019**, 31, 1804790.

[41] Z. Xiao, F. Liu, X. Geng, J. Zhang, S. Wang, Y. Xie, Z. Li, H. Yang, Y. Yuan, L. Ding, *Science bulletin* **2017**, 62, 1331.

[42] X. Wan, C. Li, M. Zhang, Y. Chen, *Chemical Society Reviews* **2020**, 49, 2828.

[43] H. Chen, Y. Zou, H. Liang, T. He, X. Xu, Y. Zhang, Z. Ma, J. Wang, M. Zhang, Q. Li, *Science China Chemistry* **2022**, 65, 1362.

[44] Y. Huang, C. Rong, R. Zhang, S. Liu, *Journal of molecular modeling* **2017**, 23, 1.

[45] Y. Mao, M. Head-Gordon, Y. Shao, *Chemical science* **2018**, 9, 8598.

[46] F. Meyers, S. R. Marder, B. M. Pierce, J.-L. Bredas, *Journal of the American Chemical Society* **1994**, 116, 10703.

[47] D. Jacquemin, C. Adamo, *Journal of chemical theory and computation* **2011**, 7, 369.

[48] T. Mikie, I. Osaka, *Journal of Materials Chemistry C* **2020**, 8, 14262.

[49] A. Bibi, S. Muhammad, S. UrRehman, S. Bibi, S. Bashir, K. Ayub, M. Adnan, M. Khalid, *ACS omega* **2021**, 6, 24602.

[50] Q. Wang, J. Qi, W. Qiao, Z. Y. Wang, *Dyes and Pigments* **2015**, 113, 160.

[51] J. Qi, W. Qiao, X. Zhou, D. Yang, J. Zhang, D. Ma, Z. Y. Wang, *Macromolecular Chemistry and Physics* **2016**, 217, 1683.

[52] L. Hu, W. Qiao, J. Han, X. Zhou, C. Wang, D. Ma, Z. Y. Wang, Y. Li, *Polymer Chemistry* **2017**, 8, 528.

[53] X. Wang, L. Lv, L. Li, Y. Chen, K. Zhang, H. Chen, H. Dong, J. Huang, G. Shen, Z. Yang, *Advanced Functional Materials* **2016**, 26, 6306.

[54] L. Hu, W. Qiao, X. Zhou, X. Zhang, D. Ma, Y. Li, Z. Y. Wang, *Polymer* **2017**, 114, 173.

[55] L. Hu, J. Han, W. Qiao, X. Zhou, C. Wang, D. Ma, Y. Li, Z. Y. Wang, *Polymer Chemistry* **2018**, 9, 327.

[56] X. Xu, X. Zhou, K. Zhou, Y. Xia, W. Ma, O. Inganäs, *Advanced Functional Materials* **2018**, 28, 1805570.

[57] P. Murto, Z. Genene, C. M. Benavides, X. Xu, A. Sharma, X. Pan, O. Schmidt, C. J. Brabec, M. R. Andersson, S. F. Tedde, *ACS Macro Letters* **2018**, 7, 395.

[58] K. Yang, J. Wang, J. Miao, J. Zhang, F. Zhang, *Journal of Materials Chemistry C* **2019**, 7, 9633.

[59] Z. Zhong, L. Bu, P. Zhu, T. Xiao, B. Fan, L. Ying, G. Lu, G. Yu, F. Huang, Y. Cao, *ACS Applied Materials & Interfaces* **2019**, 11, 8350.

[60] Z. Zhong, K. Li, J. Zhang, L. Ying, R. Xie, G. Yu, F. Huang, Y. Cao, *ACS Applied Materials & Interfaces* **2019**, 11, 14208.

[61] Y. Xia, L. E. Aguirre, X. Xu, O. Inganäs, *Advanced Electronic Materials* **2020**, 6, 1901017.

[62] Y. Zhao, T. Liu, B. Wu, S. Zhang, N. Prine, L. Zhang, S. Pang, B. Yin, L. Ye, X. Gu, *Chemistry of Materials* **2021**, 33, 3746.

[63] X. Luo, Y. Xue, J. Wu, W. Cai, D. Täuber, I. Malovicho, B. Sava, G. Cen, X. Lu, C. Zhao, *Applied Physics Letters* **2022**, 121.

[64] X. Wang, S. Gao, J. Han, Z. Liu, W. Qiao, Z. Y. Wang, *ACS Applied Materials & Interfaces* **2022**, 14, 26978.

[65] H. Lin, B. Xu, J. Wang, X. Yu, X. Du, C.-J. Zheng, S. Tao, *ACS Applied Materials & Interfaces* **2022**, 14, 34891.

[66] X. Huang, Z. Zhao, S. Chung, K. Cho, J. Lv, S. Lu, Z. Kan, *Journal of Materials Chemistry C* **2022**, 10, 17502.

[67] Z.-M. Zhong, F. Peng, L. Ying, Z.-Q. Huang, W.-K. Zhong, G. Yu, Y. Cao, F. Huang, *Chinese Journal of Polymer Science* **2023**, 41, 1629.

[68] X. Wang, Z. Y. Wang, S. Gao, J. Han, Y. Xu, Z. Liu, H. Wang, Y. Zhang, W. Qiao, *Chemical Engineering Journal* **2023**, 474, 145529.

[69] C. Zhang, A. Song, Q. Huang, Y. Cao, Z. Zhong, Y. Liang, K. Zhang, C. Liu, F. Huang, Y. Cao, *Nano-Micro Letters* **2023**, 15, 140.

[70] X. Wang, Z. Y. Wang, J. Han, H. Zhu, J. Liu, W. Qiao, *Chemical Engineering Journal* **2024**, 484, 149653.

[71] H. Zhang, M. Liu, X. Zhao, X. Ma, G. Yuan, J. Li, F. Zhang, *Applied Physics Letters* **2023**, 123.

[72] S. Gao, X. Wang, Y. Zhao, Y. Xu, W. Qiao, Z. Y. Wang, *Chemical Engineering Journal* **2024**, 489, 151377.

[73] H. Kim, J. Kang, J. Park, H. Ahn, I.-N. Kang, I. H. Jung, *Macromolecules* **2022**, 55, 9489.

[74] J. B. Barton, R. F. Cannata, S. M. Petronio, presented at Infrared Detectors and Focal Plane Arrays VII **2002**.

[75] Z. Wu, N. Li, N. Eedugurala, J. D. Azoulay, D.-S. Leem, T. N. Ng, *npj Flexible Electronics* **2020**, 4, 6.

[76] J. Kublitski, A. Hofacker, B. K. Boroujeni, J. Benduhn, V. C. Nikolis, C. Kaiser, D. Spoltore, H. Kleemann, A. Fischer, F. Ellinger, *Nature communications* **2021**, 12, 551.

[77] O. J. Sandberg, C. Kaiser, S. Zeiske, N. Zarrabi, S. Gielen, W. Maes, K. Vandewal, P. Meredith, A. Armin, *Nature Photonics* **2023**, 17, 368.

[78] H. F. Haneef, A. M. Zeidell, O. D. Jurchescu, *Journal of Materials Chemistry C* **2020**, 8, 759.

[79] H. Bässler, D. Kroh, F. Schauer, V. Nádaždy, A. Köhler, *Advanced Functional Materials* **2021**, 31, 2007738.

[80] X. Ma, H. Bin, B. T. van Gorkom, T. P. van der Pol, M. J. Dyson, C. H. Weijtens, M. Fattori, S. C. Meskers, A. J. van Breemen, D. Tordera, *Advanced Materials* **2023**, 35, 2209598.

[81] J. Onorato, V. Pakhnyuk, C. K. Luscombe, *Polymer Journal* **2017**, 49, 41.

[82] J.-W. Lee, C. Sun, S.-W. Lee, G.-U. Kim, S. Li, C. Wang, T.-S. Kim, Y.-H. Kim, B. J. Kim, *Energy & Environmental Science* **2022**, 15, 4672.

RESEARCH ARTICLE

Entry for the Table of Contents

All-polymer flexible SWIR photodetectors
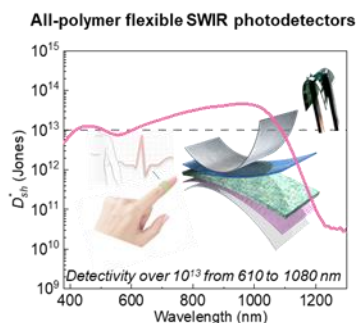
Two ultra-narrow-bandgap polymer acceptors were synthesized for construction of all-polymer short-wavelength infrared (SWIR) photodetectors. The all-polymer photodetectors achieved a high specific detectivity (D_{sh}^*) over 10^{13} Jones from 610 (visible) to 1080 nm (SWIR) under zero bias. The all-polymer flexibe photodetectors were successfully applied in heart rate monitoring, optical communication and SWIR imaging.

Institute and/or researcher Twitter usernames: @jishan_wu